

**Influence of the background state on Rossby wave propagation  
into the Great Lakes region based on observations and model  
simulations**

KATHLEEN D. HOLMAN<sup>1,2</sup> \*    DAVID J. LORENZ<sup>1</sup>

MICHAEL NOTARO<sup>1</sup>

*1. Nelson Institute Center for Climatic Research, University of Wisconsin-Madison, Madison, WI, USA.*

*2. Department of Atmospheric and Oceanic Sciences, University of Wisconsin-Madison, Madison, WI, USA.*

---

*\* Corresponding author address:* Kathleen D. Holman, Department of Atmospheric and Oceanic Sciences, University of Wisconsin-Madison 1225 W. Dayton St., Madison, WI 53706.  
E-mail: kathleendeholman@gmail.com

6 We investigate the relationship between hydrology in the Great Lakes basin, namely over-  
7 lake precipitation, and transient Rossby waves using the National Centers for Environmen-  
8 tal Predictions-National Center for Atmospheric Research (NCEP-NCAR) Reanalysis data  
9 and historical output from the third phase of the Coupled Model Intercomparison Project  
10 (CMIP3). The preferred path of observed Rossby wave trains associated with over-lake  
11 precipitation on Lake Superior depends strongly on season and appears related to the time-  
12 mean, upper-level flow. During summer and fall, the Northern Hemisphere extratropical  
13 jet is relatively sharp and acts as a waveguide, such that Rossby wave trains traversing the  
14 Great Lakes region travel along the extratropical Pacific and Atlantic jets. During other  
15 months, the Pacific jet is relatively broad, which allows more wave activity originating in  
16 the tropics to penetrate into the mid-latitudes and influence Lake Superior precipitation.  
17 Analysis of CMIP3 models is intended to 1) further our understanding of how variations  
18 in the mean state influence transient Rossby waves and 2) assess models' ability to capture  
19 observed features such as wave origin and track. Results indicate that Rossby wave train  
20 propagation in 20th century simulations can significantly differ by model. Unlike observa-  
21 tions, some models do not produce a well-defined jet across the Pacific Ocean during summer  
22 and fall. As a result, some Rossby waves affecting the Great Lakes region originate in the  
23 tropics. Collectively, observations and model results show the importance of the time-mean,  
24 upper-level flow on Rossby wave propagation and therefore, on the relative influence of the  
25 tropics versus the extratropics on the hydroclimate of the Great Lake region.

# 1. Introduction

The intersection of regional hydrology and large-scale atmospheric circulation patterns remains an active and continuously evolving area of research. Many of the previous studies involving Midwest and Great Lakes hydrology focus on the relationship with pre-defined teleconnection patterns and associated time series, such as the Pacific-North American (PNA) teleconnection pattern (Rodionov 1994; Grover and Sousounis 2002; Coleman and Rogers 2003; Ghanbari and Bravo 2008), the Atlantic Multidecadal Oscillation (Hanrahan et al. 2010), and the El Niño-Southern Oscillation (Rodionov and Assel 2000; Assel et al. 2000; Rogers and Coleman 2003). Rather than exploring the direct link between atmospheric circulations and hydrology, those studies utilize simplified versions of the atmosphere. Outside of the Great Lakes community however, there has been a recent interest in connecting regional hydrology directly to atmospheric circulations, namely through transient Rossby waves. For example, results from Ding and Wang (2005) indicate that summer precipitation over East Asia, the North Pacific, and parts of North America is related to a zonally-elongated Rossby wave packet, referred to as the circumglobal teleconnection pattern (CGT; Branstator 2002). Feldstein and Dayan (2008) identify a relationship between winter precipitation over Israel and an eastward-propagating Rossby wave that originates over the northeast Pacific. Results from Martius et al. (2008) indicate that heavy precipitation events along the Alpine south-side are preceded by Rossby wave trains throughout the year. Similarly, Wang et al. (2010) suggest that anomalously wet conditions over Utah during June 2009 were the result of a short Rossby wave train propagating along the extratropical jet stream. These studies, along with others, demonstrate that Rossby waves modulate regional climate, including precipitation, yet the relationship with hydrology in the Great Lakes region has yet to be investigated.

Rossby waves owe their existence to gradients in the potential vorticity (PV) field. Since the jet stream is associated with strong gradients in PV, Rossby waves are modified by the basic state (i.e. background flow) within which they are embedded (Hoskins and Karoly

1981; Hoskins and Ambrizzi 1993; Kosaka et al. 2009). Researchers have developed a variety of modeling experiments and observational diagnostics to understand how changes in the basic-state influence Rossby wave propagation, including barotropic models (Hoskins and Karoly 1981; Branstator 1983), baroclinic models (Held 1983; Lee and Held 1993; Yun et al. 2011), general circulation models (GCMs; Barnes and Hartmann 2011), and reanalysis data (Branstator 2002; Martius et al. 2010). Some historical modeling studies employ homogeneous or zonally-symmetric wind profiles (Hoskins et al. 1977; Opsteegh and Van den Dool 1980; Hoskins and Karoly 1981), while other approaches increase complexity by accounting for longitudinal variations in the basic-state (Branstator 1983; Karoly 1983; Hoskins and Ambrizzi 1993). Overall, results indicate that Rossby wave propagation is strongly influenced by both zonal and meridional variations in the upper-level wind field. In the absence of strong gradients in the mean background state, Rossby waves follow a great-circle path, while Rossby waves propagating within a strong jet tend to be refracted back toward the jet core resulting in zonally-oriented chains of anomalies along the axis of the jet. In other words, upper-level jet streams act as waveguides, focusing and trapping perturbations, resulting in relationships or teleconnections between widely separated regions of the globe (Branstator 2002; Martius et al. 2010).

Newman and Sardeshmukh (1998) investigate the monthly evolution of the observed Rossby waveguide, which they define by a gradient in the absolute vorticity field on an upper-level, isobaric surface. Their results indicate that the structure of the Rossby waveguide over the Pacific Ocean changes throughout the year, influencing the forcing region important for disturbances traversing the United States. For example, the United States is sensitive to forcing over the eastern Pacific during winter months, while the western Pacific becomes more important during the late spring. Based on their analysis of the absolute vorticity field, the winter Rossby waveguide is centered near  $30^{\circ}\text{N}$  and extends into the eastern Pacific, where there exists a westerly duct that allows for tropical-extratropical interactions and cross-equatorial flows (Webster and Holton 1982; Knippertz 2005). Alternatively, the average

summer waveguide is straddled by a negative absolute vorticity gradient to the north and south, blocking the westerly wind duct and steering Rossby waves across the Pacific toward the east coast of North America. These differences in the structure of the Rossby waveguide over the Pacific Ocean likely influence climatic conditions downstream.

Later studies agree with results from Newman and Sardeshmukh (1998), suggesting that the structure and location of the Rossby waveguide change with the basic state (Ding and Wang 2005; Martius et al. 2008; Yun et al. 2011). Ding and Wang (2005), for instance, consider differences in Rossby wave train paths across the Pacific Ocean during summer months (June-September). According to their analysis, Rossby wave trains follow the westerly jet in each month and migrate northward with the seasonal cycle of the jet stream. In addition, the July waveguide is weaker than the June waveguide and results in a shorter wavelength of associated Rossby wave trains. Yun et al. (2011) analyze the impact of the basic state on Rossby wave propagation in a linearized barotropic model during July and August. Their results suggest that the extratropical response to diabatic forcing in the mid-latitudes is typically larger under August conditions than July conditions, due to changes in the mean vorticity and divergence fields between the two months. Their results emphasize the importance of monthly analyses, rather than seasonal, in exploring and understanding Rossby wave propagation.

In this paper, we expand on previous research by exploring the direct relationship between precipitation in the Great Lakes region and large-scale atmospheric circulation patterns, namely atmospheric Rossby waves. We explore how variability in the upper-level wind field on a monthly timescale influences the origin and path of the Rossby waves that traverse the Great Lakes basin. To further demonstrate how variations in the basic-state influence Rossby waves that traverse the Great Lakes region, we examine transient Rossby waves simulated by 16 different GCMs that participated in the third phase of the Coupled Model Intercomparison Project (CMIP3). The analysis of simulated Rossby waves is motivated by the fact that reanalysis data represents a single realization of the atmosphere, and using multiple GCMs

with different basic-states may illuminate the effects of variations in the mean-state more easily. In addition, the analysis of simulated Rossby waves serves two primary purposes. The first is to use these models to improve our understanding of underlying relationships between Rossby waves and the upper-level mean flow, while the second is to explore models' reliability in representing these features. In light of future climate projections that suggest a strengthening and poleward shift of the extratropical jet stream (Kushner et al. 2001; Lorenz and DeWeaver 2007), results from this study may provide useful for future climate model development and assessing model uncertainty with implications for future water resources in the Great Lakes region.

The remainder of the paper is structured as follows. Section 2 includes a description of the observational datasets and model output. Analysis of observed Rossby waves that are associated with over-lake precipitation in the Great Lakes region is presented in section 3. Model-simulated Rossby waves are analyzed in section 4. Finally, section 5 contains a summary of our results.

## 2. Data

The relationship between large-scale atmospheric circulation patterns and regional hydrology in the Great Lakes basin is established using over-lake precipitation estimates from the Lake Superior basin between 1948-2010. Although direct observations of over-lake precipitation are not available, the National Oceanic and Atmospheric Administration's (NOAA) Great Lakes Environmental Research Laboratory (GLERL) estimates over-lake precipitation by applying a Thiessen polygon algorithm (Croley and Hartmann 1985) to over-land precipitation observations. Records are updated and maintained by GLERL and are publicly available through an online hydrological database (Croley and Hunter 1994). Some seasonal biases in over-lake precipitation are expected because the algorithm used to generate the estimates is based solely on land-based observations and does not incorporate variations in

atmospheric stability over the lake surface, which is related to differences in temperature between the lake surface and overlying air (Holman et al. 2012). We, however, analyze daily precipitation anomalies and perform correlation analyses on each month separately. Following Chatterjee and Goswami (2004) and Fujinami and Yasunari (2009), anomalies were constructed by removing the first three harmonics of the annual cycle. Rather than over-lake precipitation estimates, the analysis could have applied over-land precipitation measurements from the Lake Superior watershed. However, the two time series are highly correlated, such that the results would likely be very similar.

Analyses of 300 hPa zonal ( $u$ ) and meridional wind ( $v$ ) observations are based on daily data, on a  $2.5^\circ$  latitude  $\times$   $2.5^\circ$  longitude grid, from the National Centers for Environmental Prediction-National Center for Atmospheric Research (NCEP-NCAR) Reanalysis product (Kalnay et al. 1996) between 1948-2010. In addition to reanalysis data, daily output of precipitation and 300 hPa  $u$  and  $v$  wind from 16 different coupled ocean-atmosphere GCMs (Table 1) is analyzed from 1961-2000. The GCM data are part of the 20th century experiment (20C3M) from the World Climate Research Programme’s (WCRP; Meehl et al. 2007) Coupled Model Intercomparison Project Phase 3 (CMIP3). Climate simulations apply both dynamical atmosphere and ocean components. Because the horizontal resolution of model output varies from  $1.125^\circ$  latitude  $\times$   $1.125^\circ$  longitude to  $4^\circ$  latitude  $\times$   $5^\circ$  longitude, all model data were linearly interpolated to the same horizontal resolution as the NCEP-NCAR Reanalysis data. Leap days were removed from all datasets. As with the precipitation data, meridional wind anomalies were constructed as deviations of the daily mean from the first three harmonics of the annual cycle. This is done in observations and model simulations to isolate transient disturbances in the meridional wind field. The annual mean and seasonal cycle are not removed from upper-level zonal wind fields because the primary objective of this study is to demonstrate how variations in the *mean* background flow influence observed and simulated transient Rossby waves.

### 3. Observed Rossby waves

#### *a. Precipitation and 300 hPa meridional wind*

Analysis of Lake Superior’s hydrologic budget suggests that over-lake precipitation is the largest source of water to the lake on an annual basis (Lenters 2004). The seasonal cycle of over-lake precipitation estimates (Fig. 1) is characterized by a warm season peak (May-September) typical of the Midwest, United States (Holman and Vavrus 2012), with the largest (smallest) average amount observed during September (February) (Lenters 2004). The monthly standard deviation (Fig. 1) follows a similar seasonal cycle as the mean precipitation, with a minimum in February and maxima during September and June. Though studies identify a relationship between winter precipitation in the Great Lakes basin and large-scale teleconnection patterns such as the PNA pattern (Rodionov 1994; Isard et al. 2000; Coleman and Rogers 2003; Notaro et al. 2006), the average contribution of winter (DJF) precipitation to the annual total is less than 20% in the Lake Superior basin. It is, therefore, important to investigate these relationships in all seasons, rather than only winter.

We investigate the relationship between over-lake precipitation in the Lake Superior basin and transient Rossby waves through a series of time-lag correlation maps in which the daily over-lake precipitation anomaly time series is correlated with daily observed 300 hPa meridional wind anomalies at each grid point. Specific months are presented here which demonstrate key differences in Rossby wave origin and path throughout the year, including April, July, and September (Fig. 2). April, July, and September months were selected because they show a variety of path structures that exist throughout the year, while these months also show similar features to surrounding months (i.e. April is similar to March and May).

On average, during the month of April (Fig. 2a), the eddy-driven Pacific jet core is characterized by zonal winds between 35-40 m s<sup>-1</sup> across the North Pacific. Recall that the barotropic PV field associated with the background flow is related to  $-\partial^2 U / \partial y^2$ , such



184 that a narrow jet, like the climatological April Pacific jet, represents a relatively strong PV  
 185 gradient and waveguide. The subtropical Pacific jet located off the west coast of Mexico  
 186 is longitudinally elongated and extends from the International Date Line to the Southwest  
 187 United States. The eddy-driven Atlantic jet, with core speeds between 25-30 m s<sup>-1</sup>, is  
 188 oriented in a southwest-northeast direction. The subtropical Atlantic jet is characterized  
 189 by a relatively zonal orientation, with zonal wind speeds that are slightly weaker than the  
 190 eddy-driven, mid-latitude jet. Rossby waves (Fig. 2a) correlated with over-lake precipitation  
 191 during April originate over eastern Asia and propagate along a single, relatively constant  
 192 latitude band from day -4 to day -2. Day 0 correlations between over-lake precipitation  
 193 and 300 hPa meridional wind peak over the Great Lakes basin and central North America.  
 194 Beginning on day 0, the Rossby wave ray paths on the leading edge of the wave train diverge  
 195 meridionally. By day +2, the existence of two possible tracks is suggested by local correlation  
 196 maxima, although the maxima are not completely disconnected from one another.

197 The day 0 correlation map for April (Fig. 2a) indicates that positive over-lake precipita-  
 198 tion anomalies are associated with southerly winds directly overhead, with northerly winds  
 199 located to the west and east of the southerly winds. Alternative months show similar results  
 200 for day 0 correlation maps (Fig. 2b,c). This upper-level meridional wind pattern suggests  
 201 the presence of a trough-ridge couplet located over central North America, where the Great  
 202 Lakes are located downstream of the trough axis. Upper-level divergence associated with  
 203 the eastward-moving upper-level trough supports upward vertical motion near the central  
 204 US/Great Lakes region. Instantaneous correlation maps between over-lake precipitation and  
 205 sea-level pressure (SLP; not shown) indicate that over-lake precipitation is associated with  
 206 negative SLP anomalies to the southwest of Lake Superior, with positive SLP anomalies to  
 207 the southeast throughout the year. The induced pressure gradient under such conditions is  
 208 conducive for transporting warm, moist air from the Gulf of Mexico into the Great Lakes  
 209 region.

210 During July, the zonal wind structure and preferred Rossby wave path (Fig. 2b) show

211 different results. The climatological July extratropical jets are relatively weak and essentially  
 212 zonal across the entire domain, located between 35°-50°N. Regional zonal wind speed maxima  
 213 exist over the central North Pacific and near the US-Canada border, extending into the  
 214 western North Atlantic, representing the cores of the eddy-driven jets. The subtropical  
 215 branches in the North Pacific and North Atlantic are, however, essentially absent. Rossby  
 216 waves associated with over-lake precipitation in July originate over the western North Pacific  
 217 and propagate along a single path within the extratropical Pacific jet between day -4 and  
 218 day 0. As with other months, the correlation coefficients are maximized on day 0 over central  
 219 North America, including the Great Lakes basin. However, Rossby waves in July, as with the  
 220 other summer months (June and August, not shown), remain trapped in the extratropical  
 221 Atlantic jet beyond day 0, without propagation into the subtropics. The existence of a  
 222 narrow jet over the North Pacific and North Atlantic helps to trap and focus perturbations  
 223 in the midlatitude waveguide, as suggested by Branstator (2002) and Schwierz et al. (2004).

224 During December (Fig. 2c), the climatological eddy-driven Pacific jet is stronger than  
 225 the April and July mean state, with average zonal speeds up to 60 m s<sup>-1</sup>. A subtropical jet  
 226 is located off the west coast of Mexico, with average zonal speeds that are much weaker than  
 227 the central North Pacific jet. The eddy-driven Atlantic jet is also relatively strong during  
 228 December, reaching speeds close to 40 m s<sup>-1</sup>. The mean Atlantic jet is located over the east  
 229 coast of the United States and is characterized by a slight southwest-northeast orientation.  
 230 On average, Rossby waves that traverse the Great Lakes region during December (Fig. 2c)  
 231 appear to originate over two different locations (day -4): the poleward flank of the Pacific  
 232 jet near 60°N, which could be a relatively weak Arctic jet, and the equatorward flank of the  
 233 Pacific jet, in the western central subtropical Pacific near 25°N. The two paths converge over  
 234 the Gulf of Alaska and develop a meridional wind anomaly downstream over central North  
 235 America (day -4 to day 0). By day 0, correlation coefficients between over-lake precipitation  
 236 and meridional wind are maximized over the Great Lakes region and central North America.  
 237 Beyond day 0, two propagation paths appear, including a northeastward track trapped in

the Atlantic jet and a potential subtropical path that tracks towards Africa.

The strongest correlations between over-lake precipitation anomalies and 300 hPa meridional wind anomalies occur on day 0 for each month (Fig. 3). Correlation values in Fig. 3 are based on locating the maximum correlation value anywhere within the domain shown in Fig. 2, regardless of location<sup>1</sup>. There exists a noticeable seasonal cycle in the relationship between precipitation and upper-level meridional wind, where the strongest correlations are observed during the transition seasons, such as April and October, and the weakest correlations are observed during winter months. Winter months may be characterized by the weakest correlations due to the frequent occurrence of smaller-scale precipitation events, such as lake-effect snow (Norton and Bolsenga 1993; Notaro et al. 2013). Transition seasons may be characterized by the largest correlations due to the frequent occurrence of synoptic-scale forcing, rather than convective events which occur most often during the summer months.

#### *b. 300 hPa Meridional wind*

Observed Rossby waves that traverse the Great Lakes basin are further analyzed using a series of time-lag correlation maps in which the time series of daily 300 hPa meridional wind anomalies at a single point is correlated with meridional wind anomalies at every grid point (Fig. 4), an approach used by others to identify and explore Rossby waves (Chang 1993; Branstator 2002; Hakim 2003). This analysis is done to explore all Rossby waves that traverse the Great Lakes region, rather than isolating only those waves associated with over-lake precipitation. We chose a base point of 50.0°N, 267.5°E (southwest Ontario, Canada) in the 300 hPa meridional wind field because this location is characterized by the largest instantaneous (i.e. day 0) positive correlation between over-lake precipitation and 300 hPa meridional wind throughout the year (or it is located adjacent to the point with the maximum value), and would likely have the strongest relationship with water resources in the Great

---

<sup>1</sup>We identified the largest correlation value rather than picking a specific grid cell and identifying the largest correlation value at that point. Identified locations varied between 50-52.5°N and 267.5-270°E.

Lakes basin. The correlation coefficients of the wave trains displayed in Fig. 4a are larger than those identified using over-lake precipitation anomalies (Fig. 2) because the waves are identified by correlating two meridional wind time series.

Since the Rossby waves identified using the aforementioned meridional wind base point were all very similar in phase to those presented in Fig. 2 (although with greater amplitude), we present a single month, April, to avoid redundancy. On average, April Rossby wave trains that traverse the Great Lakes region originate over eastern Asia (Fig. 4a) and propagate along a single track across the North Pacific from day -4 to day -2, similar to the transient Rossby waves that influence over-lake precipitation during this month. Beyond day -2, the leading nodes spread meridionally, ultimately leading to the existence of two possible tracks by day +2. As with the other time-lag correlation plots presented here, the maximum correlation value ( $r=1$ ) is reached on day 0.

Hovmöller diagrams, which have been employed in many studies of transient atmospheric waves (Hovmöller 1949; Matthews 2000), are presented to highlight differences among observed Rossby waves that traverse the Great Lakes basin during different times of the year (Fig. 5). For an example of composite Hovmöller diagrams, see Martius et al. (2008). Here, the Hovmöller diagrams were calculated by correlating 300 hPa meridional wind anomalies at the base point ( $50.0^{\circ}\text{N}$ ,  $267.5^{\circ}\text{E}$ ) with 300 hPa meridional wind anomalies averaged over  $35^{\circ}$ - $55^{\circ}\text{N}$ . This latitude band was selected to emphasize transient Rossby waves propagating within the extratropics. Based on the Hovmöller diagram, April Rossby waves (Fig. 5a) develop near  $120^{\circ}\text{E}$ , approximately five days prior to traversing the Great Lakes region. Wave packets retain structure in the defined latitude band for about nine days, ceasing beyond  $330^{\circ}\text{E}$ . On average, July Rossby wave trains (Fig. 5b) develop near  $180^{\circ}\text{W}$ , three to four days prior to traversing the Upper Midwest, and retain a coherent structure for approximately eight days. The December wave packet (Fig. 5c) shows minimal structure west of  $180^{\circ}\text{E}$ , and lasts for approximately one week, although the negative and positive anomaly couplet located near  $230^{\circ}\text{E}$  persists for nearly two weeks. This persistent feature likely represents

the high temporal autocorrelation in the meridional wind field over the Aleutian islands (Croci-Maspoli et al. 2007) and western United States.

The theoretical dispersion relation for non-stationary, non-divergent Rossby waves linearized about the zonal wind is shown in Eq. 1. The dispersion relation is based on assuming that the fluid is barotropic and of constant depth, and the Rossby wave is an absolute vorticity-conserving motion. Eq. 1 indicates that the zonal phase velocity ( $C = \frac{\omega}{k}$ ) and zonal group velocity ( $C_{gx} = \frac{\partial \omega}{\partial k}$ ) depend on the background flow, where  $\omega$  is the frequency of the wave,  $U$  is the zonal wind speed,  $\beta$  is the meridional gradient in absolute vorticity, and  $k$  and  $l$  are the zonal and meridional wavenumbers, respectively.

$$\omega = Uk - \frac{\beta k}{(k^2 + l^2)} \quad (1)$$

Previous studies suggest that the zonal phase velocity of midlatitude transient waves is related to lower to mid-tropospheric zonal winds between 500-850 hPa, while the zonal group velocity of such waves is related to upper tropospheric zonal winds between 200-400 hPa (Berbery and Vera 1996; Chang and Yu 1999).

Empirical estimates of  $C$  were calculated by quantifying the change in longitude of the maximum positive regression coefficient near the base point longitude (267.5°E) from day -1 to day +1 in monthly Hovmöller regression diagrams (not shown). Because the coarse horizontal resolution of the NCEP-NCAR Reanalysis dataset limits accurate distance calculations, we used a parabola to better estimate the location of the maximum on day -1 and day +1. More specifically, we first identified the maximum point and two surrounding points on day -1 and day +1 and then fit a parabola to those three points for each day separately.  $C$  was quantified as the distance traveled by the maxima in the two parabolas over that time. The empirical estimates of  $C$  (Fig. 6) show little variability across seasons, ranging from 7.4 m s<sup>-1</sup> in June to 9.9 m s<sup>-1</sup> in November. These values agree with previous estimates for Northern Hemisphere midlatitude waves by Randel and Held (1991) and Chen et al. (2008), although with lower seasonal variability than expected. Perhaps seasonal fluctuations in the

basic-state have a larger influence on the path of Rossby wave packets rather than phase speeds.

Hovmöller regression plots were also used to estimate monthly values of  $C_{gx}$ . First, the location of the maximum of the wave envelope was calculated on day -2 and day +2, where the wave envelope was calculated using the Hilbert transform of correlation coefficients across longitude (Zimin et al. 2003). For a complete description of the Hilbert transform, see Section 4. As with the calculations of  $C$ , a parabola was used to estimate the actual longitude of the wave envelope maximum on day -2 and day +2.  $C_{gx}$  was calculated as the distance traveled by the wave envelope maximum over those four days. Unlike the empirical estimates of  $C$ , estimates of  $C_{gx}$  (Fig. 6) show a seasonal cycle that generally resembles the seasonal cycle of average 300 hPa zonal wind speeds, with larger values observed during winter and lower values observed during summer. The largest values of  $C_{gx}$  occur during January and February, with an additional relative maximum in August. The Hovmöller diagrams and empirical estimates of  $C$  and  $C_{gx}$  highlight differences in wave characteristics throughout the year.

## 4. Simulated Rossby waves

We analyze 20th century climate model output from 16 different GCMs (Table 1) that participated in the IPCC Fourth Assessment Report (Meehl et al. 2007) to further demonstrate how variations in the upper-level zonal wind structure influence the path of transient Rossby waves that traverse the Great Lakes region. We analyze these simulations for two main purposes. The first purpose is to use these models as a tool to illustrate how variations in the average 300 hPa zonal-wind structure may impact transient Rossby waves, and the second purpose is to qualitatively assess models' abilities to reproduce the observed origin region and path of Rossby waves that traverse the Great Lakes region. Simulated Rossby waves that are associated with Great Lakes precipitation and that traverse the Great Lakes

region were identified in each of the models using similar techniques to the analysis above. To understand the simulated relationship between precipitation and transient Rossby waves, we first averaged the daily precipitation time series from the grid cell closest to Lake Superior (48°N, 272°E) with four grid cells directly adjacent to it (totaling five grid cells), for each month separately. We computed time-lag correlation maps between simulated precipitation and 300 hPa meridional wind for each month and model, although we present the multi-model average for a single month, July, and single lag value, day 0, for brevity (Fig. 7a). We focus the analysis of simulated Rossby waves on the month of July because warm-season precipitation dominates the observed seasonal cycle and results may have implications for water resources.

Figure 7a shows the multi-model average day 0 correlation map between daily precipitation anomalies and 300 hPa meridional wind anomalies for all July months between 1961-2000, along with the multi-model mean July 300 hPa zonal winds. The multi-model zonal wind structure shows regional maxima over the western North Pacific and over the eastern United States and western North Atlantic, although zonal wind speeds are lower than observations in the core of the Pacific jet and along the poleward flank of the Atlantic jet by about  $4 \text{ m s}^{-1}$ . As with observations (Fig. 2b), the multi-model average correlation map between precipitation and 300 hPa meridional wind indicates that simulated precipitation in the Great Lakes region is associated with a Rossby wave train located across North America, with positive precipitation anomalies associated with southerly winds directly overhead that are straddled to the east and west by northerly winds. The phasing of the upper-level meridional winds is similar to observations, putting the Great Lakes region on the downstream side of an upper-level trough.

Recall that observed Rossby waves associated with over-lake precipitation in the Great Lakes basin appeared very similar in phase to those Rossby waves related to 300 hPa meridional wind variations near the defined base point (50°N, 267.5°E). Similar results are true for the climate model simulations. Figure 7b illustrates the July multi-model average instantana-

neous correlation map between daily 300 hPa meridional wind anomalies at 50°N, 267.5°E and 300 hPa meridional wind anomalies at all other grid cells. The phasing in Figure 7b is very similar to Figure 7a, though the magnitudes are greater in Figure 7b (maximum correlation of 1.0 versus 0.44). The spatial scale of the positive and negative correlations in Figure 7b are also larger than Figure 7a, likely due to the large spatial autocorrelation in the upper-level wind field.

Because the magnitudes of correlations in Fig. 7 are greater using a meridional wind base point, we continue to explore how simulated variations in the upper-level flow field influence transient Rossby waves that traverse the Great Lakes region using correlation maps based solely on 300 hPa meridional wind. We present a multi-model composite analysis of simulated time-lag correlation maps for the month of July to illustrate differences in Rossby wave features among models. A more objective analysis between the upper-level zonal wind field and transient Rossby waves can be found below. Composites are based on identifying models (Table 1) with above-average (Fig. 8a) and below-average (Fig. 8b) zonal wind component at 300 hPa within the eastern fringe of the North Pacific extratropical jet (40°-52.5°N, 180°-150°W; black box in Fig. 8a, b), where above- and below-average are relative to the multi-model mean. There are eight models in each composite. The above- (below-) average composite represents an elongated and stronger (contracted and weaker) extratropical Pacific jet.

Composites in Fig. 8a indicate that models with above-average zonal wind speeds south of the Aleutian Islands are characterized by a uniform extratropical Pacific jet, with relatively constant zonal wind from the east coast of China to the west coast of North America. Average zonal wind speeds in the eddy-driven Atlantic jet ( $>20 \text{ m s}^{-1}$ ) are stronger than the Pacific jet ( $10\text{-}15 \text{ m s}^{-1}$ ). Zonal wind speeds in the above-average composite are greater than the reanalysis data (Fig. 8c) in the latitude band between 20°N and 45°N. Average simulated zonal wind speeds are lower over the northeastern North Pacific, across the western half of Canada (near 50°N), and over the North Atlantic, between western North American and



eastern Europe ( $55^{\circ}$ - $60^{\circ}$ N). On average, simulated Rossby wave trains in the above-average pool of models originate over eastern Asia and western North Pacific (day -6) and propagate along the extratropical jet stream with little meridional deviation from day -6 to day 0.

Models with below-average zonal wind speeds south of the Aleutian Islands produce differing results. The multi-model average 300 hPa zonal wind structure is characterized by weaker zonal winds across the entire extratropical North Pacific and North Atlantic Oceans, as compared to the above-average composite. The eddy-driven Pacific jet appears disconnected from the jet over central Canada, while the multi-model average includes a relatively weak ( $<10 \text{ m s}^{-1}$ ) subtropical jet located off southwest coast of North America, a feature that is absent in the above-average composite. Relative to reanalysis data (Fig. 8c), zonal winds in the below-average composite are weaker in the core of the observed Pacific and Atlantic jets by 7 and 4  $\text{m s}^{-1}$ , respectively. The below-average composite shows subtropical zonal winds south of  $30^{\circ}$ N that exceed reanalysis data across most of the domain presented in Fig. 8b. Unlike observations and the above-average composite, simulated Rossby wave trains in these models show, on average, two preferred origins: the tropical North Pacific Ocean, south of the Hawaiian islands (day -6), and the central North Pacific Ocean (day -4). The two paths merge over the eastern North Pacific Ocean and propagate as a single wave train across North America.

July time-lag correlation maps based on the NCEP-NCAR Reanalysis data (Fig. 8c) indicate the transient Rossby waves that traverse the Great Lakes region originate over the western North Pacific Ocean (day -4) and propagate across North America (day -2) and the North Atlantic (day 0), within the eddy-driven jets. The wave structure shows little sign of subtropical or tropical origin.

The July composite analysis suggests that the climatological structure of the 300 hPa zonal wind field influences the origin and propagation path of transient Rossby waves that traverse the Upper Midwest in 20th century GCM simulations. However, potential differences in the phase of waves due to differences in wavelength among models may limit the

robustness of such composites. In fact, close inspection of individual time-lag correlation maps indicates that differences in zonal and meridional wavelengths exist among the CMIP3 models, ultimately impacting wave phase. Consequently, averaging correlation fields that contain positive and negative features across different models may reduce the amplitude of resulting waves. To avoid this, the Hilbert transform was applied to each model’s time-lag correlation maps to identify and track the Rossby Wave Envelopes (RWEs). The Hilbert transform of a real array,  $x_r$ , returns a real array,  $x_h$ , that is the original data where each wave number is phase shifted by  $90^\circ$  (Ouerqli 2002; Strong and Liptak 2012). The returned array,  $x_h$ , has the same frequency and amplitude as the original data,  $x_r$ . The wave envelope is identified by calculating the square root of the sum of the squared real component and phase-shifted component [ $x_e = \sqrt{x_r^2 + x_h^2}$ ]. The units and scale of the resulting array,  $x_e$ , are the same as the original time series (correlation coefficients), and values are all greater than or equal to zero, thereby eliminating concern of wave cancellation. In the current analysis, the Hilbert transform is applied to spatial correlation maps and represents a *proxy* for Rossby wave activity, which is not to be confused with the dynamical definition of wave activity (e.g. Plumb 1986). Previous examples of applying the Hilbert transform in space can be found in Zimin et al. (2003), Danielson et al. (2006), Ambaum and Athanasiadis (2007), and Ambaum (2008).

An example of the Hilbert transform applied to observed time-lag correlation maps (Fig. 4b) demonstrates the effect on the Rossby wave train. As described above, the observed time-lag correlation maps for April (Fig. 4a) indicate the Rossby wave train originates over eastern Asia and propagates along the extratropical Pacific jet from day -4 to day -2. Beyond day -2, the leading nodes expand meridionally and follow two possible tracks, a northern track propagating along the eddy-driven Atlantic jet and a southern track propagating toward the west coast of Africa. The RWEs identified using the Hilbert transform (Fig. 4b) capture the spatial extent of the Rossby wave train as it propagates eastward along the extratropical jets and into the tropics. By day +2, the RWE captures a regional maximum over the tropical

North Atlantic ( $\sim 15^\circ\text{N}$ ) and off the east coast of North America ( $\sim 45^\circ\text{N}$ ), corresponding to the two tracks previously mentioned. Thus, the RWEs in Fig. 4b, in conjunction with previous applications (Zimin et al. 2003; Ambaum and Athanasiadis 2007), suggest the Hilbert transform is a useful tool for approximating the location and propagation of transient Rossby wave trains.

Rather than re-doing the composite analysis using RWEs, we expand our analysis to further illustrate how simulated variations in the background flow are related to variations in Rossby waves using Maximum Covariance Analysis (MCA). MCA, sometimes referred to as Singular Value Decomposition, is a statistical technique used to identify patterns of covariability between time series of two different variables (Bretherton et al. 1992; Wallace et al. 1992). MCA involves calculating a covariance matrix between two variables over a sampling dimension. In the current analysis, we evaluate patterns of covariability between model-simulated mean 300 hPa zonal winds and model-simulated day -3 RWEs within the region bounded by  $110^\circ\text{E}$ - $300^\circ\text{E}$ ,  $0^\circ$ - $70^\circ\text{N}$ , the Pacific-North American region. MCA was repeated using a number of smaller 300 hPa zonal wind domains, which resulted in very little change to the dominant patterns of covariability and statistical significance, and verified the robustness of our findings. Day -3 RWEs were chosen to emphasize differences in upstream characteristics of simulated Rossby wave trains among models. Before computing the covariance matrix, the multi-model mean of both variables was removed, and both variables were weighted by the square root of the cosine of latitude.

Unlike most MCA studies (Bretherton et al. 1992; Deser and Timlin 1997), the covariance matrix was calculated over the model dimension (16 GCMs), rather than the time dimension, for each month separately. This is similar to the approach presented by Delcambre et al. (2013a) and Delcambre et al. (2013b). Because the current MCA analysis samples across model space rather than time, identified patterns are not equivalent to temporal variability of any single model. Instead, the patterns represent inter-model variability of climatological 300 hPa zonal wind speed anomalies that are associated with day -3 RWE anomalies. MCA

results for the leading mode of covariability are presented in the form of heterogeneous regression patterns, in which model-simulated 300 hPa zonal wind speed is regressed onto the day -3 RWE expansion coefficients and model-simulated day -3 RWEs are regressed onto the 300 hPa zonal wind expansion coefficients. MCA results for two individual months, July and December, are presented to illustrate differences in the influence of the basic-state on transient Rossby waves.

The strength of coupling between the two (left and right) heterogeneous regression patterns for each month is measured by the squared covariance fraction (SCF) and the normalized squared covariance (NSC) (Table 2). The SCF, defined by Bretherton et al. (1992), represents the amount of covariance explained by each mode, though we present results for the first mode only. Values range from a minimum of 46% in March to a maximum of 73% in November. The NSC corresponds to the ratio between the squared covariance represented by the first mode and the square-root of the product of the area-integrated variance in the two fields (Wallace et al. 1992; Santos et al. 2007). Wallace et al. (1992) suggest that NSC values above 0.1 represent strong coupling, although large values of NSC together with small values of shared covariance likely have little meaning. Monthly values of the NSC (Table 2) range from 0.28 in April to 0.38 in September. Finally, the significance of the correlations between the left and right expansion coefficients (Table 2) was tested using a Monte Carlo approach, in which the left and right fields were randomly paired before computing the covariance matrix. We performed 1000 random iterations for each month. Significant correlations based on the 95th percentile of the Monte Carlo correlation distribution include nine of the 12 months and are shown in bold in Table 2.

MCA results for July (Fig. 9c,d) indicate that models characterized by above-average 300 hPa zonal wind speeds across the extratropical North Pacific and United States (30-45°N), concurrent with slightly below-average zonal wind speeds in the subtropical North Pacific (15-25°N), are associated with above average Rossby wave activity over the North Pacific. The RWE anomaly pattern represents a westward expansion of the multi-model maximum

located off the northwest coast of North America (Fig. 9b). Conversely, models with slightly above average zonal wind speeds across the subtropical North Pacific and below average zonal wind speeds across the extratropical North Pacific and United States are accompanied by above-average Rossby wave activity emanating from the central tropical Pacific and below-average wave activity upstream of the multi-model maximum on day -3. These results, which agree with the multi-model July composites (Fig. 8a,b), suggest that stronger winds in the extratropical jet tend to increase the strength of the extratropical waveguide. Wave activity over the Great Lakes region is, therefore, more likely to originate in the Pacific jet in this case. Conversely, in the presence of weaker winds in the extratropical jet, the extratropical waveguide is weakened and therefore, wave activity over the Great Lakes tends to trace a more great circle-like path that originates in the tropical Pacific. The tropical versus extratropical origin of simulated Rossby wave activity is not unique to July, but also exists during August (not shown).

December MCA results differ from summer findings, yet closely resemble the patterns identified during November, January, and February. The December heterogeneous zonal wind pattern (Fig. 10c) indicates that models with above-average zonal wind speeds across the subtropics, including above-average zonal winds in the Pacific jet entrance and exit regions, and reduced wind speeds to the north and south of the subtropical belt are associated with increased wave activity emanating from the tropical central Pacific Ocean and less wave activity in the western Pacific jet stream (Fig. 10d).

To determine whether the differences in the background state are in fact causing the differences in the wave propagation, we integrate the linearized barotropic vorticity equation (2) backward in time for three days, starting from the lag 0 regression map. The model is linearized about three different background states. The first background state used was the latitudinally- and longitudinally-varying rotational component of the multi-model mean zonal and meridional wind, while the second and third background states were the multi-model mean wind plus or minus the winds regressed on the zonal wind expansion co-

528 efficient (i.e. plus or minus the anomalous left MCA pattern). The initial condition for the  
529 streamfunction is calculated from the meridional wind regression pattern at lag 0 under the  
530 assumption that all of the flow is rotational. The linearized barotropic equation is standard,  
531 except for the fact that the sign of the diffusion is reversed so that small scale features that  
532 develop are removed when the model is run *backwards*:

$$\frac{\partial \zeta}{\partial t} + \frac{U}{a \cos(\theta)} \frac{\partial \zeta}{\partial \lambda} + \frac{V}{a} \frac{\partial \zeta}{\partial \theta} + \frac{u}{a \cos(\theta)} \frac{\partial Z}{\partial \lambda} + \frac{v}{a} \frac{\partial (f + Z)}{\partial \theta} + \nu \nabla^2 \zeta = 0 \quad (2)$$

533 where  $\zeta$ ,  $u$  and  $v$  are the wave relative vorticity, zonal wind and meridional wind, respec-  
534 tively,  $Z$ ,  $U$  and  $V$  are the background relative vorticity, zonal wind and meridional wind,  
535 respectively,  $\lambda$  is the longitude,  $\theta$  is the latitude,  $a$  is the radius of the earth,  $f$  is the  
536 Coriolis parameter and  $\nu$  is the diffusivity. Note that the vorticity equation above only  
537 involves the absolute/relative vorticity and not the potential vorticity. We believe that the  
538 absolute vorticity is more relevant because the waves are likely better described as equiv-  
539 alent barotropic external Rossby waves (Held et al. 1985), rather than waves localized in  
540 the vertical in the vicinity of the tropopause. The propagation of external Rossby waves is  
541 governed by the winds and absolute vorticity at the “equivalent barotropic level” in the mid-  
542 to upper-troposphere (Held et al. 1985). We find that a better simulation is achieved if the  
543 background state is taken from the 400 hPa instead of the 300 hPa level. This is in better  
544 agreement with the equivalent barotropic level calculated from the Northern Hemisphere  
545 background state (Held et al. 1985). Since the meridional wind regression pattern at 400  
546 hPa is essentially proportional to the regression pattern at 300 hPa, and the model is linear  
547 in the waves, we simply use the 300 hPa lag 0 regression map as the initial condition to  
548 predict the 300 hPa lag -3 regression map. The model resolution is T63 and the time step is  
549 18 minutes using a third order Adams-Bashforth scheme. The value of the diffusivity is such  
550 that the smallest resolved wave is damped with an  $e$ -folding time of six hours. The model  
551 is integrated backwards in time for three days and the resulting meridional wind is first

normalized by the local meridional wind standard deviation to allow a direct comparison to the correlation maps. Finally, the normalized meridional wind is used to calculate the RWE in the same way as in the model diagnostics described above.

The RWE at day -3 for the model-mean background flow is shown for July (Fig. 11a) and December (Fig. 11b). These figures should be compared with Fig. 9b and Fig. 10b, respectively. For July, the location and amplitude of the modelled RWE peak generally agree with the average climate model RWE, although the modelled RWE has a second relatively weak maximum southeast of the main peak that is not present in the climate models. For December, the modelled RWE has two main peaks: one in the northeast Pacific and one in the western Pacific, much like the climate models. Like July, however, the modelled RWE has an additional relatively weak maximum in the southeast Pacific that is not present in the climate models. The amplitude of the modelled RWE in December is also too large, but we believe the spatial patterns are more important because the amplitude can be adjusted by simply changing the diffusivity in the modelled model.

To produce a result analogous to the MCA results, we take half the difference between the modelled simulation with the background from the model mean winds *plus* the anomalous MCA winds and the simulation with the background from the model mean winds *minus* the anomalous MCA winds. Differences in the RWE for July and December are shown in Fig. 11c and 11d, respectively. These figures should be compared with Fig. 9d and Fig. 10d. For July, the modelled RWE difference pattern shows positive anomalies in the central Pacific and negative anomalies further east. This pattern is like that of the climate model MCA pattern, except that the negative climate model pattern extends deeper into the subtropics and less into northwest Canada. For December, the modelled RWE difference pattern shows two main positive centers: one in the northeast Pacific and one in the central, subtropical Pacific. There is one main negative center in the western Pacific with a narrow tongue extending eastward to separate the two main positive centers. These features are remarkably similar to the MCA pattern from the climate models. These barotropic model simulations

suggest that, to first order, changes in the background horizontal flow are responsible for the variations in wave propagation in the climate models and that differences in baroclinicity and differences in the structure of the wave packets at lag 0 are less important.

## 5. Discussion and Conclusions

In this analysis we have expanded on previous research by exploring the direct connection between Great Lakes hydrology and large-scale atmospheric circulations. More specifically, we have examined the relationship between over-lake precipitation in the Lake Superior basin and transient Rossby waves using 300 hPa meridional winds. Observations between 1948-2010 show that over-lake precipitation in the Lake Superior basin is related to transient Rossby waves during each month of the year. The strongest correlations between over-lake precipitation estimates and 300 hPa meridional wind occur during the transition months of April and October, while the weakest correlations occur during winter months, when over-lake precipitation amounts are relatively small. One explanation for the weaker correlations during winter months may be the occurrence of lake-effect snow events. Since lake-effect snow events are largely determined by regional features like ice cover and temperature differences between the lake surface and overlying atmosphere (Notaro et al. 2013), the relationship with large-scale atmospheric circulations may be reduced. Summer values are likely reduced to the occurrence of smaller-scale, convective events. Regardless of month, the instantaneous correlation maps consistently reveal a positive relationship between over-lake precipitation anomalies and an upper-level trough-ridge couplet over central North America, with positive precipitation anomalies associated with southerly winds directly overhead.

Although similarities among over-lake precipitation and meridional wind correlation maps exist, there are noticeable differences in observed Rossby wave paths throughout the year. For example, winter months are typically characterized by two different paths, both upstream over the North Pacific and downstream of the Great Lakes region, over the North



Atlantic. Summer months, however, consistently produce a single path, both upstream and downstream of the Great Lakes basin. Summer disturbances propagate within the Pacific and Atlantic eddy-driven jets, or waveguides, throughout their entire life cycle. The shoulder season months represent more of a hybrid between winter and summer conditions, commonly capturing a single track upstream of the focus region and dual tracks downstream. Time-lag correlation maps between 300 hPa meridional wind at a single point (defined in relation to over-lake precipitation in the Lake Superior basin) and the 300 hPa meridional wind at all other grid cells agree well with the correlation maps based on over-lake precipitation and 300 hPa meridional wind, further supporting the influence of the mean state on transient Rossby waves.

In addition to Lake Superior relations, time-lag correlation maps were produced between over-lake precipitation estimates from the other four Great Lakes (Michigan, Huron, Erie, and Ontario) and 300 hPa meridional wind anomalies between 1948-2010. Based on cross-correlations, the over-lake precipitation time series for the Lake Superior basin is most (least) correlated with over-lake precipitation from the Lake Michigan (Erie) basin, in agreement with the winter cross-correlations presented by Rodionov (1994). As such, the time-lag correlation maps between over-lake precipitation from the Lake Michigan basin and 300 hPa meridional winds are very similar to those presented for Lake Superior. The most noticeable differences occur during winter months (DJF), when correlations between over-lake precipitation and upper-level meridional winds are weakest for both lakes. Monthly time-lag correlation maps based on over-lake precipitation anomalies in the Lake Erie basin qualitatively resemble those for Lake Superior; however, the amplitudes are less than those observed using the Lake Superior precipitation anomalies and the meridional wavelengths of the Rossby waves are slightly smaller. Since the focus of the current study is on the Great Lakes region, further research is warranted to explore the impact of the background flow on transient waves around the globe.

Beyond observations, output from 16 CMIP3 models was analyzed to further demonstrate

how variations in the simulated upper-level zonal wind field influence the origin and propagation path of transient Rossby waves that affect precipitation and traverse the central United States. Multi-model average time-lag correlation maps between simulated precipitation and 300 hPa meridional wind closely resemble the correlation maps defined solely using 300 hPa meridional wind, though correlations between precipitation and 300 hPa meridional wind were weaker. As such, the model analysis focused primarily on understanding differences in Rossby wave characteristics among models using the later maps. Two different approaches, a multi-model composite and maximum covariance analysis, were used to demonstrate the influence the background flow has on disturbances that traverse the Great Lakes basin.

Results from model simulations suggest that the structure of the time-mean, upper-level flow influences Rossby wave propagation across the Pacific Ocean, North America, and Atlantic Ocean, ultimately impacting the relative influence of the tropics and extratropics on the hydroclimate of the Great Lake region. The July multi-model composite analysis shows that models with above-average zonal winds in the extratropical jet more closely resemble the reanalysis data and show RWEs propagating along the extratropical jet, within the waveguide, both upstream and downstream of the Great Lakes region. Alternatively, models that simulate below-average zonal winds in the extratropical jet are characterized by more wave activity reaching the Great Lakes region from a tropical path, rather than originating within the extratropics. Further research is needed to understand the hydrological implications of such vastly different origin regions for the Rossby waves traversing the Great Lakes region.

In addition to the multi-model composite analysis, maximum covariance analysis was utilized to identify patterns of covariability between model-simulated 300 hPa zonal winds and day -3 Rossby wave envelopes during July and December. July MCA results agree with the composite analysis, showing that models with above-average 300 hPa zonal wind speeds in the region between 30°-45°N and simultaneous below-average zonal wind speeds in the subtropical belt between 15° -25°N show more wave activity emanating from within

the extratropics and less from the tropics. MCA results for December suggest that models with above-average zonal wind speeds between  $15^{\circ}$  -  $30^{\circ}$ N, straddled by below-average zonal wind speeds to the north and south, show more wave activity emanating from the tropics. Conversely, models with above-average zonal wind speeds between  $30^{\circ}$  -  $55^{\circ}$ N and the equator to  $10^{\circ}$ N show more wave activity originating over eastern Asia and the western Pacific Ocean.

Experiments with a barotropic model linearized about the background flow reproduce the results of the MCA patterns to a remarkable degree and further support our hypothesis that changes in the background horizontal flow are responsible for the variations in the origin of wave packets, and that differences in baroclinicity and the structure of wave packets while they are over the Great Lakes region are less important.

Collectively, results from this analysis illustrate the relationship between hydrology in the Great Lakes basin and the large-scale atmospheric circulation, including the influence of the tropics on extratropical waves. Based on these findings, one could hypothesize that simulated tropical Pacific Ocean conditions may influence Great Lakes precipitation variability in models with weak waveguides. Since water levels in the Great Lakes basin are integrative, lake levels are more sensitive to low-frequency precipitation variability and the processes which influence precipitation variability. Future changes to the climate system, including a projected poleward shift of the extratropical jets (Lorenz and DeWeaver 2007; Delcambre et al. 2013a) and expansion of the tropical Hadley Cell (Lu et al. 2007; Johanson and Fu 2009) under increased concentrations of greenhouse gases, will likely have important consequences for the water resources in the Great Lakes region.

#### *Acknowledgments.*

We acknowledge Tim Hunter, from NOAA's Great Lakes Environmental Research Laboratory, for providing the over-lake precipitation estimates. We acknowledge the modeling groups, the Program for Climate Model Diagnosis and Intercomparison (PCMDI), and the WCRP's Working Group on Coupled Modeling (WGCM) for their roles in mak-

ing available the WCRP CMIP3 multi-model dataset. Support of this dataset is provided by the Office of Science, U.S. Department of Energy. NCEP-NCAR Reanalysis data provided by the NOAA/OAR/ESRL PSD, Boulder, Colorado, USA, from their website at <http://www.esrl.noaa.gov/psd/>. This study was funded by the Michigan Department of Natural Resources through the Environmental Protection Agency Great Lakes Restoration Initiative grant.

## REFERENCES

- Ambaum, M., 2008: Unimodality of wave amplitude in the Northern Hemisphere. *J. Atmos. Sci.*, **65** (3), 1077–1086.
- Ambaum, M. and P. Athanasiadis, 2007: The response of a uniform horizontal temperature gradient to heating. *J. Atmos. Sci.*, **64** (10), 3708–3716.
- Assel, R., J. Janowiak, D. Boyce, C. O’Connors, F. Quinn, and D. Norton, 2000: Laurentian Great Lakes ice and weather conditions for the 1998 El Niño winter. *Bull. Amer. Meteor. Soc.*, **81** (4), 703–717.
- Barnes, E. and D. Hartmann, 2011: Rossby wave scales, propagation, and the variability of eddy-driven jets. *J. Atmos. Sci.*, **68** (12), 2893–2908.
- Berbery, E. and C. Vera, 1996: Characteristics of the Southern Hemisphere winter storm track with filtered and unfiltered data. *J. Atmos. Sci.*, **53** (3), 468–481.
- Branstator, G., 1983: Horizontal energy propagation in a barotropic atmosphere with meridional and zonal structure. *J. Atmos. Sci.*, **40** (7), 1689–1708.

705 Branstator, G., 2002: Circumglobal teleconnections, the jet stream waveguide, and the North  
706 Atlantic Oscillation. *J. Climate*, **15** (14), 1893–1910.

707 Bretherton, C., C. Smith, and J. Wallace, 1992: An intercomparison of methods for finding  
708 coupled patterns in climate data. *J. Climate*, **5** (6), 541–560.

709 Chang, E., 1993: Downstream development of baroclinic waves as inferred from regression  
710 analysis. *J. Atmos. Sci.*, **50** (13), 2038–2053.

711 Chang, E. and D. Yu, 1999: Characteristics of wave packets in the upper troposphere. Part  
712 I: Northern Hemisphere winter. *J. Atmos. Sci.*, **56** (11), 1708–1728.

713 Chatterjee, P. and B. N. Goswami, 2004: Structure, genesis and scale selection of the tropical  
714 quasi-biweekly mode. *Quarterly J. of the Roy. Meteor. Soc.*, **130** (599), 1171–1194.

715 Chen, G., J. Lu, and D. Frierson, 2008: Phase speed spectra and the latitude of surface  
716 westerlies: Interannual variability and global warming trend. *J. Climate*, **21** (22), 5942–  
717 5959.

718 Coleman, J. and J. Rogers, 2003: Ohio River Valley winter moisture conditions associated  
719 with the Pacific-North American teleconnection pattern. *J. Climate*, **16** (6), 969–981.

720 Croci-Maspoli, M., C. Schierz, and H. Davies, 2007: A multifaceted climatology of atmo-  
721 spheric blocking and its recent linear trend. *J. Climate*, **20** (4), 633–649.

722 Croley, T. and H. Hartmann, 1985: Resolving Thiessen polygons. *J. Hydrology*, **76** (3-4),  
723 363–379.

724 Croley, T. and T. Hunter, 1994: Great Lakes Monthly Hydrologic Data. *NOAA Technical*  
725 *Memorandum ERL GLERL-83*.

726 Danielson, R., J. Gyakum, and D. Straub, 2006: A case study of downstream baroclinic  
727 development over the North Pacific Ocean. Part II: Diagnoses of eddy energy and wave  
728 activity. *Mon. Wea. Rev.*, **134** (5), 1549–1567.

- Delcambre, S. C., D. Lorenz, D. Vimont, and J. Martin, 2013a: Diagnosing Northern Hemisphere jet portrayal in 17 CMIP3 global climate modesl: Twentieth century inter-model variability. *J. Climate*, **26**, 4910–4929.
- Delcambre, S. C., D. Lorenz, D. Vimont, and J. Martin, 2013b: Diagnosing Northern Hemisphere jet portrayal in 17 CMIP3 global climate modesl: Twenty-first century projections. *J. Climate*, **26**, 4930–4946.
- Deser, C. and M. Timlin, 1997: Atmosphere-ocean interaction on weekly timescales in the North Atlantic and Pacific. *J. Climate*, **10** (3), 393–408.
- Ding, Q. and B. Wang, 2005: Circumglobal teleconnection in the Northern Hemisphere summer\*. *J. Climate*, **18** (17), 3483–3505.
- Feldstein, S. and U. Dayan, 2008: Circumglobal teleconnections and wave packets associated with Israeli winter precipitation. *Q. J. R. Meteorol. Soc.*, **134** (631), 455–467.
- Fujinami, H. and T. Yasunari, 2009: The effects of midlatitude waves over and around the Tibetan Plateau on submonthly variability of the East Asian summer monsoon. *Mon. Wea. Rev.*, **137** (7), 2286–2304.
- Ghanbari, R. and H. Bravo, 2008: Coherence between atmospheric teleconnections, Great Lakes water levels, and regional climate. *Adv. in Wat. Res.*, **31** (10), 1284–1298.
- Grover, E. and P. Sousounis, 2002: The influence of large-scale flow on fall precipitation systems in the Great Lakes Basin. *J. Climate*, **15** (14), 1943–1956.
- Hakim, G., 2003: Developing wave packets in the North Pacific storm track. *Mon. Wea. Rev.*, **131** (11), 2824–2837.
- Hanrahan, J., S. Kravtsov, and P. Roebber, 2010: Connecting past and present climate variability to the water levels of Lakes Michigan and Huron. *Geo. Res. Lett.*, **37** (1), L01701.

753 Held, I., 1983: Stationary and quasi-stationary eddies in the extratropical troposphere:  
754 Theory. *Large-Scale Dynamical Processes in the Atmosphere*, B. J. Hoskins and R. P.  
755 Pearce, Eds., Academic Press, 127–168.

756 Held, I. M., R. L. Panetta, and R. T. Pierrehumbert, 1985: Stationary external Rossby  
757 waves in vertical shear. *J. Atmos. Sci.*, **42** (9), 865–883.

758 Holman, K., A. Gronewold, M. Notaro, and A. Zarrin, 2012: Improving historical precipita-  
759 tion estimates over the Lake Superior basin. *Geo. Res. Lett.*, **39** (3), L03405.

760 Holman, K. and S. Vavrus, 2012: Understanding simulated extreme precipitation events in  
761 Madison, Wisconsin and the role of moisture flux convergence during the late 20th and  
762 21st centuries. *J. Hydrometeor.*, **13** (3), 877–894.

763 Hoskins, B. and T. Ambrizzi, 1993: Rossby wave propagation on a realistic longitudinally  
764 varying flow. *J. Atmos. Sci.*, **50** (12), 1661–1671.

765 Hoskins, B. and D. Karoly, 1981: The steady linear response of a spherical atmosphere to  
766 thermal and orographic forcing. *J. Atmos. Sci.*, **38** (6), 1179–1196.

767 Hoskins, B., A. Simmons, and D. Andrews, 1977: Energy dispersion in a barotropic atmo-  
768 sphere. *Quarterly J. of the Roy. Meteor. Soc.*, **103** (438), 553–567.

769 Hovmöller, E., 1949: The Trough-and-Ridge diagram. *Tellus*, **1** (2), 62–66.

770 Isard, S., J. Angel, and G. VanDyke, 2000: Zones of origin for Great Lakes cyclones in North  
771 America, 1899-1996. *Mon. Wea. Rev.*, **128** (2), 474–485.

772 Johanson, C. and Q. Fu, 2009: Hadley cell widening: Model simulations versus observations.  
773 *J. Climate*, **22** (10), 2713–2725.

774 Kalnay, E., et al., 1996: The NCEP/NCAR 40-year reanalysis project. *Bull. Amer. Meteor.*  
775 *Soc.*, **77** (3), 437–471.

- 776 Karoly, D., 1983: Rossby wave propagation in a barotropic atmosphere. *Dyn. of Atm. and*  
777 *Ocn.*, **7** (2), 111–125.
- 778 Knippertz, P., 2005: Tropical-extratropical interactions associated with an Atlantic tropical  
779 plume and subtropical jet streak. *Mon. Wea. Rev.*, **133** (9), 2759–2776.
- 780 Kosaka, Y., H. Nakamura, M. Watanabe, and M. Kimoto, 2009: Analysis on the dynamics of  
781 a wave-like teleconnection pattern along the summertime Asian jet based on a reanalysis  
782 dataset and climate model simulations. *J. of the Meteo. Soc. of Japan*, **87** (3), 561–580.
- 783 Kushner, P., I. Held, and T. Delworth, 2001: Southern Hemisphere atmospheric circulation  
784 response to global warming. *J. Climate*, **14** (10), 2238–2249.
- 785 Lee, S. and I. Held, 1993: Baroclinic wave packets in models and observations. *J. Atmos.*  
786 *Sci.*, **50** (10), 1413–1428.
- 787 Lenters, J., 2004: Trends in the Lake Superior water budget since 1948: A weakening seasonal  
788 cycle. *J. of Great Lakes Res.*, **30** (1), 20–40.
- 789 Lorenz, D. and E. DeWeaver, 2007: Tropopause height and zonal wind response to global  
790 warming in the IPCC scenario integrations. *J. of Geo. Res.*, **112** (D10), D10 119.
- 791 Lu, J., G. Vecchi, and T. Reichler, 2007: Expansion of the Hadley cell under global warming.  
792 *Geophys. Res. Lett.*, **34** (6), L06 805.
- 793 Martius, O., C. Schwierz, and H. Davies, 2008: Far-upstream precursors of heavy precipita-  
794 tion events on the Alpine south-side. *Quarterly J. of the Roy. Meteo. Soc.*, **134**, 417–428.
- 795 Martius, O., C. Schwierz, and H. Davies, 2010: Tropopause-level waveguides. *J. Atmos. Sci.*,  
796 **67** (3), 866–879.
- 797 Matthews, A., 2000: Propagation mechanisms for the Madden-Julian Oscillation. *Quarterly*  
798 *J. of the Roy. Meteo. Soc.*, **126** (569), 2637–2651.



- Meehl, G., C. Covey, T. Delworth, M. Latif, B. McAvaney, J. Mitchell, R. Stouffer, and K. Taylor, 2007: The WCRP CMIP3 multi-model dataset: A new era in climate change research. *Bull. Amer. Meteor. Soc.*, **88**, 1383–1394.
- Newman, M. and P. Sardeshmukh, 1998: The impact of the annual cycle on the North Pacific/North American response to remote low-frequency forcing. *J. Atmos. Sci.*, **55** (8), 1336–1353.
- Norton, D. and S. Bolsenga, 1993: Spatiotemporal trends in lake effect and continental snowfall in the Laurentian Great Lakes, 1951-1980. *J. Climate*, **6** (10), 1943–1956.
- Notaro, M., W. Wang, and W. Gong, 2006: Model and observational analysis of the northeast US regional climate and its relationship to the PNA and NAO patterns during early winter. *Mon. Wea. Rev.*, **134**, 3479–3505.
- Notaro, M., A. Zarrin, S. Vavrus, and V. Bennington, 2013: Simulation of heavy lake-effect snowstorms across the Great Lakes Basin by RegCM4: Synoptic climatology and variability. *Mon. Wea. Rev.*, **141**, 1990–2014.
- Opsteegh, J. and H. Van den Dool, 1980: Seasonal differences in the stationary response of a linearized primitive equation model: Prospects for long-range weather forecasting?. *J. Atmos. Sci.*, **37**, 2169–2185.
- Ouerqli, A., 2002: Hilbert transform from wavelet analysis to extract the envelope of an atmospheric mode: Examples. *J. of Atmos. and Oceanic Technol.*, **19** (7), 1082–1086.
- Plumb, R., 1986: Three-dimensional propagation of transient quasi-geostrophic eddies and its relationship with the eddy forcing of the time-mean flow. *J. Atmos. Sci.*, **43** (16), 1657–1678.
- Randel, W. and I. Held, 1991: Phase speed spectra of transient eddy fluxes and critical layer absorption. *J. Atmos. Sci.*, **48** (5), 688–697.

823 Rodionov, S., 1994: Association between winter precipitation and water level fluctuations in  
824 the Great Lakes and atmospheric circulation patterns. *J. Climate*, **7** (11), 1693–1706.

825 Rodionov, S. and R. Assel, 2000: Atmospheric teleconnection patterns and severity of winters  
826 in the Laurentian Great Lakes basin. *Atmos.-Ocean*, **38** (4), 601–635.

827 Rogers, J. and J. Coleman, 2003: Interactions between the Atlantic Multidecadal Oscillation,  
828 El Niño/La Niña, and the PNA in winter Mississippi valley stream flow. *Geophys. Res.*  
829 *Lett.*, **30** (10), 1518.

830 Santos, J., J. Corte-Real, U. Ulbrich, and J. Palutikof, 2007: European winter precipitation  
831 extremes and large-scale circulation: A coupled model and its scenarios. *Theo. and App.*  
832 *Clim.*, **87** (1), 85–102.

833 Schwierz, C., S. Dirren, and H. Davies, 2004: Forced waves on a zonally aligned jet stream.  
834 *J. Atmos. Sci.*, **61** (1), 73–87.

835 Strong, C. and J. Liptak, 2012: Propagating atmospheric patterns associated with Midwest  
836 winter precipitation. *J. Hydrometeor.*, **13** (4), 1371–1382.

837 Wallace, J., C. Smith, and C. Bretherton, 1992: Singular value decomposition of wintertime  
838 sea surface temperature and 500-mb height anomalies. *J. Climate*, **5** (6), 561–576.

839 Wang, S., L. Hipps, R. Gillies, X. Jiang, and A. Moller, 2010: Circumglobal teleconnection  
840 and early summer rainfall in the US Intermountain West. *Theo. and App. Clim.*, **102** (3),  
841 245–252.

842 Webster, P. and J. Holton, 1982: Cross-equatorial response to middle-latitude forcing in a  
843 zonally varying basic state. *J. Atmos. Sci.*, **39** (4), 722–733.

844 Yun, K., S. Kim, K. Ha, and M. Watanabe, 2011: Effects of subseasonal basic state changes  
845 on Rossby wave propagation during northern summer. *J. Geo. Res.*, **116** (D24), D24 102.

846 Zimin, A., I. Szunyogh, D. Patil, B. Hunt, and E. Ott, 2003: Extracting envelopes of Rossby  
847 wave packets. *Mon. Wea. Rev.*, **131** (5), 1011–1017.

## List of Tables

- 1 Coupled ocean-atmosphere GCMs from the CMIP3 (Meehl et al. 2007). Models from the above-average July composite (Fig. 8a) are indicated by (\*). 36
- 2 Squared covariance fraction (SCF), normalized squared covariance (NSC) and correlation coefficient ( $r$ ) between the 300 hPa zonal wind (left) and RWE (right) expansion coefficients for the leading mode of covariability. Bold values are significant at the 95% confidence interval based on 1000 Monte Carlo simulations. 37

TABLE 1. Coupled ocean-atmosphere GCMs from the CMIP3 (Meehl et al. 2007). Models from the above-average July composite (Fig. 8a) are indicated by (\*).

	Institute	Model	Resolution
1	Canadian Centre for Climate Modeling & Analysis	CGCM3.1(T47)*	T47
2	Canadian Centre for Climate Modeling & Analysis	CGCM3.1(T63)*	T63
3	Meteo-France / Centre National de Recherches Meteorologiques	CNRM-CM3	T42
4	CSIRO Atmospheric Research	CSIRO Mk3.0	T42
5	CSIRO Atmospheric Research	CSIRO Mk3.5	T63
6	US Dept. of Commerce, NOAA, Geophysical Fluid Dynamics Laboratory	GFDL CM2.0*	$2.5^\circ \times 2.5^\circ$
7	NASA, Goddard Institute for Space Studies	GISS-AOM*	$4^\circ \times 3^\circ$
8	NASA, Goddard Institute for Space Studies	GISS-ER	$4^\circ \times 3^\circ$
9	Institute for Applied Physics	IAP FGOALS-g1.0	$2.8^\circ \times 2.8^\circ$
10	Instituto Nazionale di Geofisica e Vulcanologia	INGV-ECHAM4	T42
11	Institute for Numerical Mathematics	INM-CM3.0	$5^\circ \times 5^\circ$
12	Center for Climate System Research (The University of Tokyo), National Institute for Environmental Studies, and Frontier Research Center for Global Change (JAMSTEC)	MIROC3.2(hires)	T106
13	Center for Climate System Research (The University of Tokyo), National Institute for Environmental Studies, and Frontier Research Center for Global Change (JAMSTEC)	MIROC3.2(medres)	T42
14	Meteorological Institute of the University of Bonn, Meteorological Research Institute of KMA, and Model and Data group	MIUB*	$4.0^\circ \times 3.75^\circ$
15	Max Planck Institute for Meteorology	MPI-ECHAM5-OM*	T63
16	Meteorological Research Institute	MRI-CGCM2.3.2*	T42

TABLE 2. Squared covariance fraction (SCF), normalized squared covariance (NSC) and correlation coefficient ( $r$ ) between the 300 hPa zonal wind (left) and RWE (right) expansion coefficients for the leading mode of covariability. Bold values are significant at the 95% confidence interval based on 1000 Monte Carlo simulations.

Month	SCF	NSC	$r(\text{left,right})$	$r_S$
Jan	58%	0.33	<b>0.93</b>	
Feb	59%	0.30	0.82	
Mar	46%	0.30	<b>0.90</b>	
Apr	49%	0.28	0.81	
May	53%	0.31	0.83	
Jun	63%	0.32	<b>0.91</b>	
Jul	63%	0.32	<b>0.90</b>	
Aug	47%	0.31	<b>0.93</b>	
Sep	67%	0.38	<b>0.88</b>	
Oct	60%	0.34	<b>0.92</b>	
Nov	73%	0.36	<b>0.90</b>	
Dec	63%	0.37	<b>0.94</b>	

## List of Figures

- 1 Average monthly estimates of over-lake precipitation ( $\text{mm d}^{-1}$ ; bars) and associated monthly standard deviation ( $\text{mm d}^{-1}$ ; line) in the Lake Superior basin between 1948-2010 based on estimates from NOAA's Great Lakes Environmental Research Laboratory. 42
- 2 Time-lag correlation maps (contours) between daily over-lake precipitation anomalies and observed 300 hPa meridional wind anomalies during (a) April, (b) August, and (c) December for four different lead/lag values. Negative (positive) lag values indicate the meridional wind anomalies precede (follow) the over-lake precipitation anomalies. The contour interval is 0.05, with positive (negative) correlations shown in red (blue) and the zero line is omitted. Correlation values greater/less than  $\pm 0.04$  are significant at the 95% confidence level, based on the Student's two-tailed t-test. Shading indicates average monthly 300 hPa zonal wind speed ( $\text{m s}^{-1}$ ) between 1948-2010. 43
- 3 Maximum zero-lag correlation between daily over-lake precipitation anomalies in the Lake Superior basin and 300 hPa meridional wind anomalies within the domain  $120^{\circ}\text{E}$ - $360^{\circ}\text{W}$ ,  $0^{\circ}$ - $70^{\circ}\text{N}$ , for each month separately between 1948-2010. All correlations are statistically significant at the 95% confidence interval based on the Student's two-tailed t-test. 44

- 875 4 (a) Time-lag correlation maps between daily 300 hPa meridional wind anoma-  
876 lies at 50.0°N, 267.5°E (black dot) and 300 hPa meridional wind anomalies  
877 at each grid cell during all Aprils between 1948-2010 based on NCEP-NCAR  
878 Reanalysis data. Positive (negative) correlations are shown in red (blue). (b)  
879 Rossby Wave Envelope (RWE) of time-lag correlation maps in (a) calculated  
880 using the Hilbert transform (Ouerqli 2002). Negative (positive) lag values in-  
881 dicate the meridional wind anomalies precede (follow) the base point. Contour  
882 interval is 0.1 with the zero line omitted. Shading indicates the climatological  
883 April 300 hPa zonal wind ( $\text{m s}^{-1}$ ) between 1948-2010. 45
- 884 5 Hovmöller diagram displaying the correlation between observed daily 300 hPa  
885 meridional wind anomaly time series at 50.0°N, 267.5°E and daily 300 hPa  
886 meridional wind anomalies averaged over 35°N-55°N during (a) April, (b)  
887 July, and (c) December, between 1948-2010. The vertical axis represents the  
888 lag value in days, while the horizontal axis represents longitude. Positive  
889 (negative) lag values indicate the base point leads (lags). Contour interval is  
890 0.1. Positive (negative) correlations are shown in red (blue) and the zero line  
891 is omitted. 46
- 892 6 Average daily 300 hPa zonal wind speed ( $\text{m s}^{-1}$ ) averaged over 40°-55°N and  
893 230°-300°E (vertical bars), along with empirical estimates of monthly zonal  
894 phase velocity ( $C$ ; filled squares) and group velocity ( $C_{gx}$ ; dash-dot line) based  
895 on NCEP-NCAR reanalysis data between 1948-2010. 47



- 896 7 Multi-model average day 0 July one-point correlation map between daily 300  
897 hPa meridional wind anomalies at each grid cell and a base point of (a) daily  
898 precipitation averaged around five grid cells centered on the Lake Superior grid  
899 cell, 48°N, 272°E, and (b) daily 300 hPa meridional wind at 50.0°N, 267.5°E  
900 during 1961-2000. Contour interval is 0.05. Positive (negative) correlations  
901 are shown in red (blue), and the zero line is omitted. Shading indicates the  
902 multi-model average July 300 hPa zonal wind speed ( $\text{m s}^{-1}$ ) between 1961-  
903 2000. Correlation values greater/less than  $\pm 0.05$  are significant at the 95%  
904 confidence level, based on the Student's two-tailed t-test. 48
- 905 8 Multi-model composite of July time-lag correlation maps (base point 50.0°N,  
906 267.5°E; identified by the black dot) for models with (a) above- and (b) below-  
907 average 300 hPa zonal wind in the region outlined by the black box (40°-  
908 52.5°N and 180°-150°W) between 1961-2000. There are eight models in each  
909 pool. (c) Observed July time-lag correlation maps (contours) between daily  
910 300 hPa meridional wind at 50.0°N, 267.5°E and 300 hPa meridional wind  
911 anomalies at every point between 1948-2010. The contour interval is 0.05 and  
912 positive (negative) correlations are shown in red (blue). Shading represents  
913 the average 300 hPa zonal wind ( $\text{m s}^{-1}$ ) (a, b) among models and (c) from  
914 NCEP-NCAR reanalysis. 49

915	9	July results from MCA of simulated 300 hPa zonal wind and day -3 RWEs.	
916		Multi-model average of mean July (a) 300 hPa zonal wind ( $\text{m s}^{-1}$ ) and (b)	
917		Day -3 RWE of one-point correlation map between 1961-2000. (c) Hetero-	
918		geneous map of 300 hPa zonal wind regressed onto day -3 RWE expansion	
919		coefficients. Red (blue) contours represent positive (negative) perturbation	
920		isotachs in units of $1 \text{ m s}^{-1}$ , with the zero-line omitted. (d) Heterogeneous	
921		map of day -3 RWE patterns regressed onto 300 hPa zonal wind expansion	
922		coefficients. Red (blue) contours represent positive (negative) correlation per-	
923		turbations in units of 0.01, with the zero-line omitted.	50
924	10	Same as Fig. 9, except for December.	51
925	11	(a) The RWE at day -3 from the barotropic model with a background state	
926		from the multi-model mean in July. (b) Same as (a) but for December. The	
927		contour interval is 0.05. (c) The July difference in RWE at day -3 from the	
928		barotropic model with background winds from the multi-model mean plus	
929		the MCA pattern and the barotropic model with background winds from the	
930		multi-model mean minus the MCA pattern. The pattern is divided by two	
931		to allow direct comparison with the MCA analysis. (d) Same as (c) but for	
932		December. Red (blue) contours represent positive (negative) values. The	
933		contour interval is 0.01, and the zero-line omitted.	52

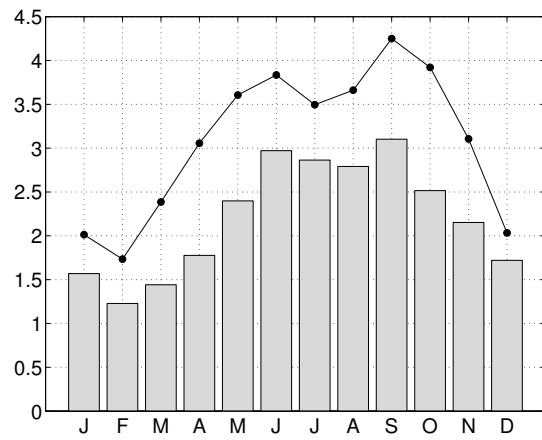


FIG. 1. Average monthly estimates of over-lake precipitation ( $\text{mm d}^{-1}$ ; bars) and associated monthly standard deviation ( $\text{mm d}^{-1}$ ; line) in the Lake Superior basin between 1948-2010 based on estimates from NOAA's Great Lakes Environmental Research Laboratory.

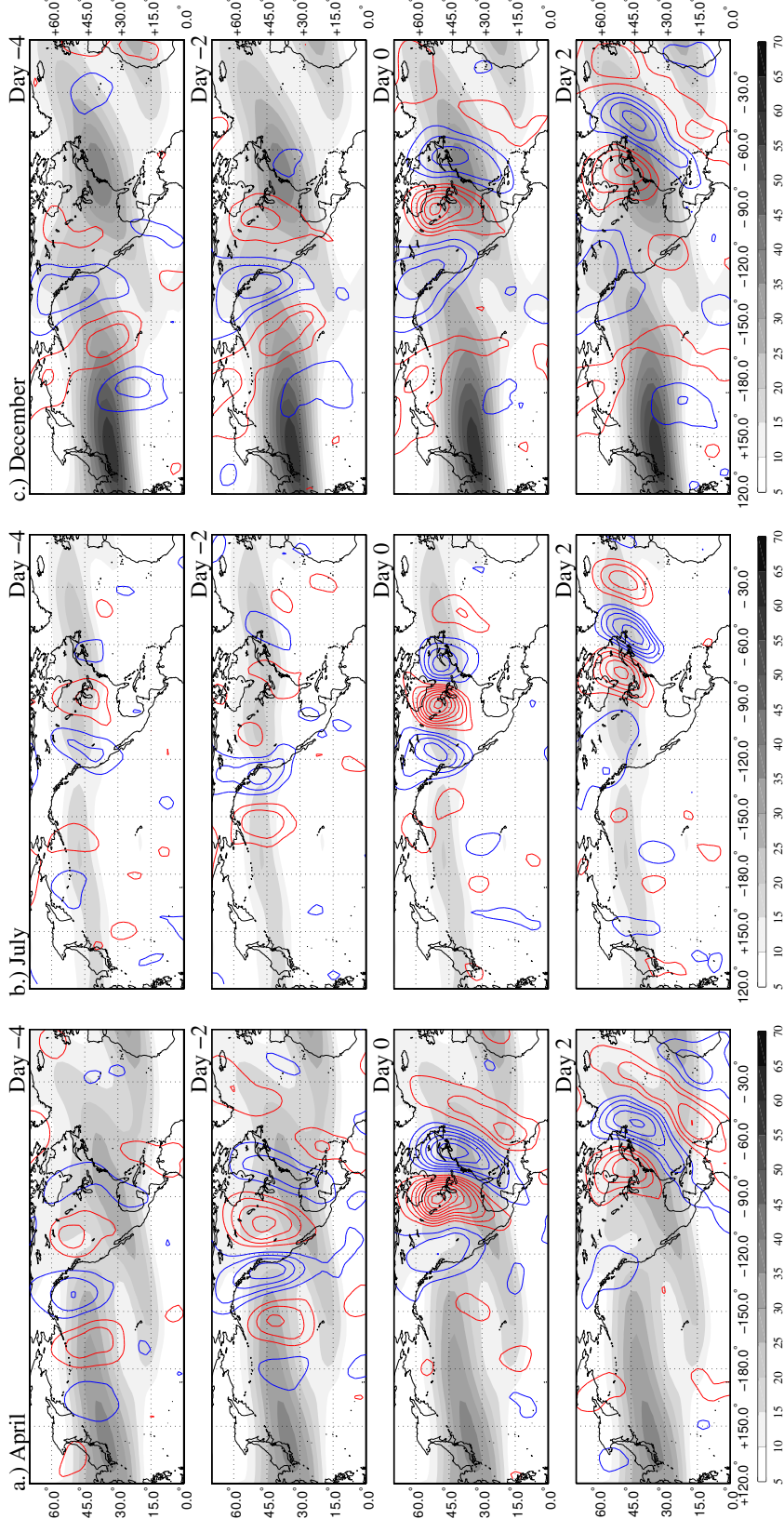


FIG. 2. Time-lag correlation maps (contours) between daily over-lake precipitation anomalies and observed 300 hPa meridional wind anomalies during (a) April, (b) August, and (c) December for four different lead/lag values. Negative (positive) lag values indicate the meridional wind anomalies precede (follow) the over-lake precipitation anomalies. The contour interval is 0.05, with positive (negative) correlations shown in red (blue) and the zero line is omitted. Correlation values greater/less than  $\pm 0.04$  are significant at the 95% confidence level, based on the Student's two-tailed t-test. Shading indicates average monthly 300 hPa zonal wind speed ( $\text{m s}^{-1}$ ) between 1948–2010.

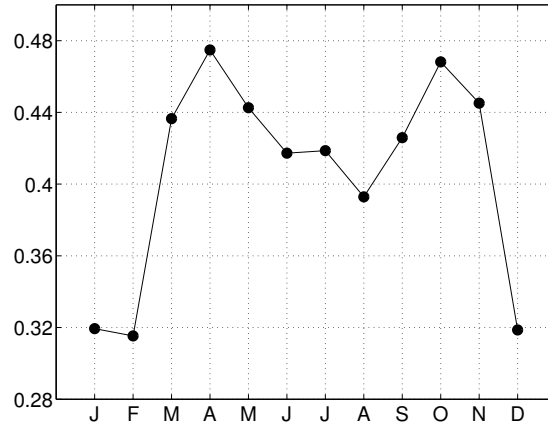


FIG. 3. Maximum zero-lag correlation between daily over-lake precipitation anomalies in the Lake Superior basin and 300 hPa meridional wind anomalies within the domain  $120^{\circ}\text{E}$ - $360^{\circ}\text{W}$ ,  $0^{\circ}$ - $70^{\circ}\text{N}$ , for each month separately between 1948-2010. All correlations are statistically significant at the 95% confidence interval based on the Student's two-tailed t-test.

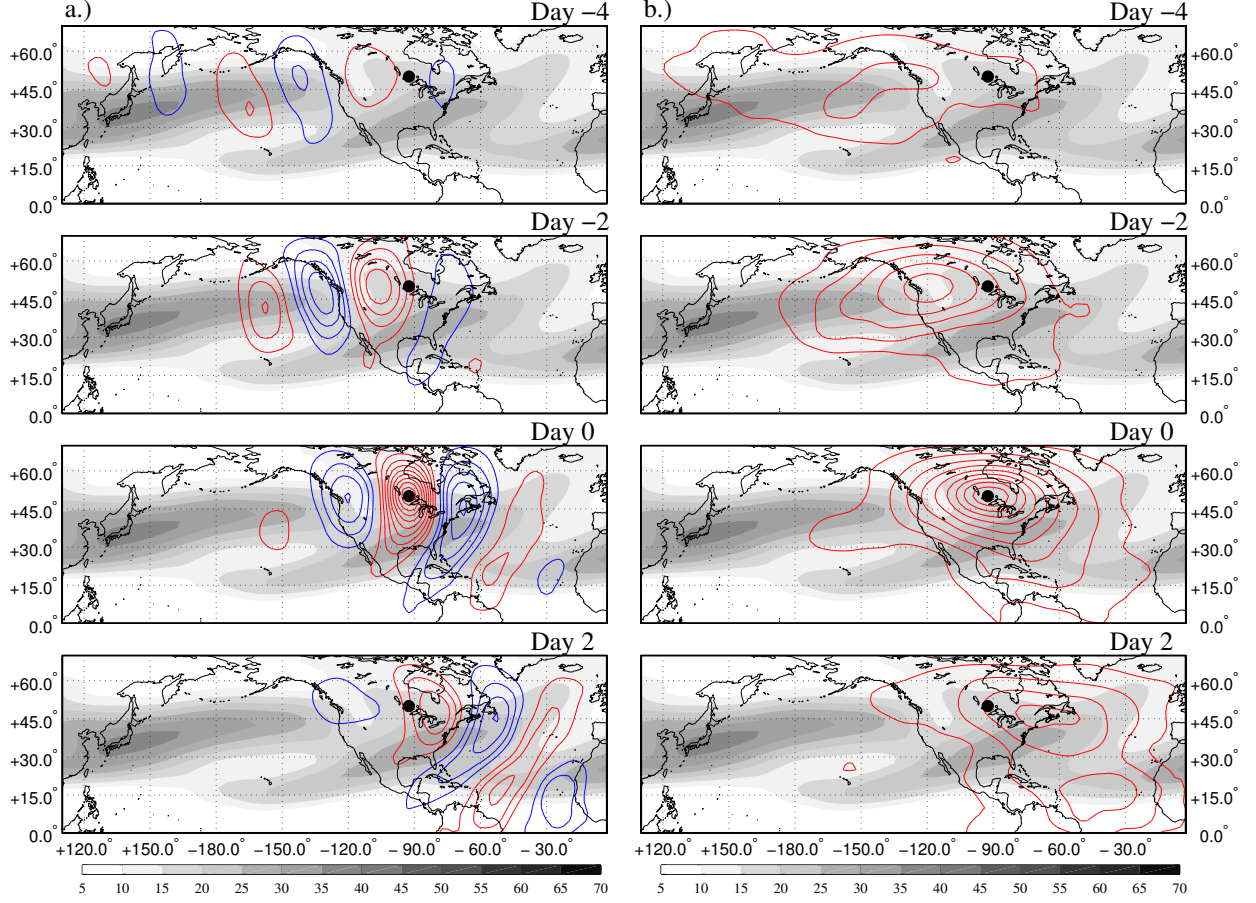


FIG. 4. (a) Time-lag correlation maps between daily 300 hPa meridional wind anomalies at  $50.0^{\circ}\text{N}$ ,  $267.5^{\circ}\text{E}$  (black dot) and 300 hPa meridional wind anomalies at each grid cell during all Aprils between 1948-2010 based on NCEP-NCAR Reanalysis data. Positive (negative) correlations are shown in red (blue). (b) Rossby Wave Envelope (RWE) of time-lag correlation maps in (a) calculated using the Hilbert transform (Ouerqli 2002). Negative (positive) lag values indicate the meridional wind anomalies precede (follow) the base point. Contour interval is 0.1 with the zero line omitted. Shading indicates the climatological April 300 hPa zonal wind ( $\text{m s}^{-1}$ ) between 1948-2010.

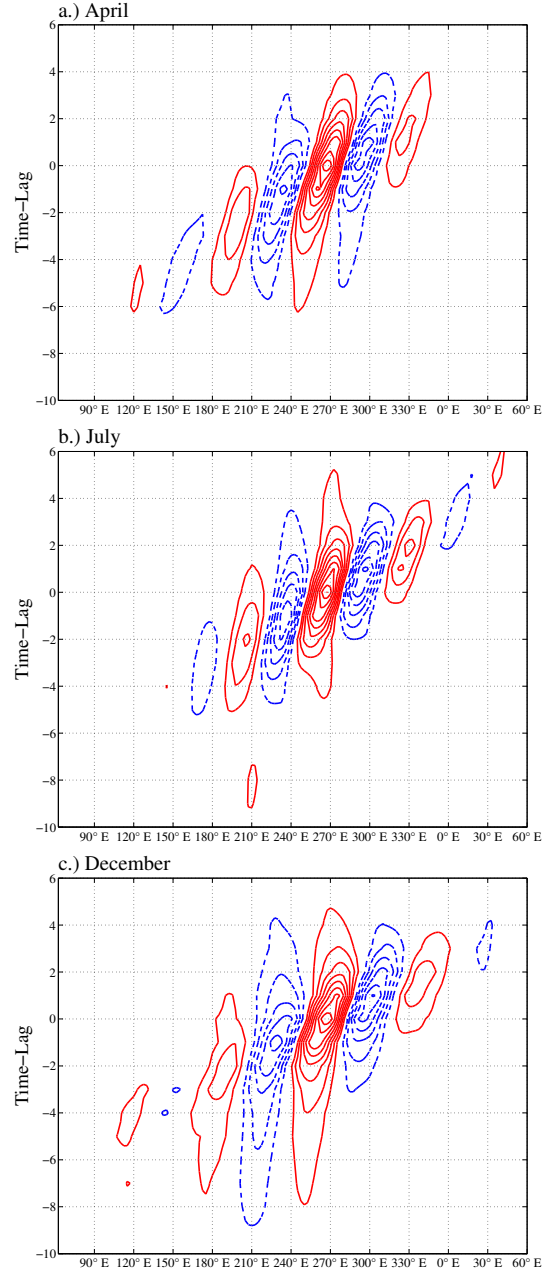


FIG. 5. Hovmöller diagram displaying the correlation between observed daily 300 hPa meridional wind anomaly time series at 50.0°N, 267.5°E and daily 300 hPa meridional wind anomalies averaged over 35°N-55°N during (a) April, (b) July, and (c) December, between 1948-2010. The vertical axis represents the lag value in days, while the horizontal axis represents longitude. Positive (negative) lag values indicate the base point leads (lags). Contour interval is 0.1. Positive (negative) correlations are shown in red (blue) and the zero line is omitted.

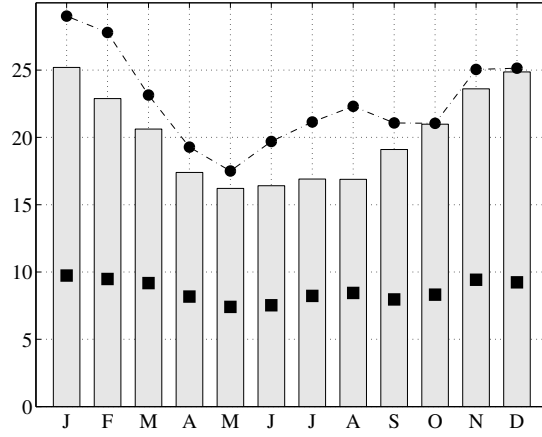


FIG. 6. Average daily 300 hPa zonal wind speed ( $\text{m s}^{-1}$ ) averaged over  $40^{\circ}$ - $55^{\circ}\text{N}$  and  $230^{\circ}$ - $300^{\circ}\text{E}$  (vertical bars), along with empirical estimates of monthly zonal phase velocity ( $C$ ; filled squares) and group velocity ( $C_{gx}$ ; dash-dot line) based on NCEP-NCAR reanalysis data between 1948-2010.



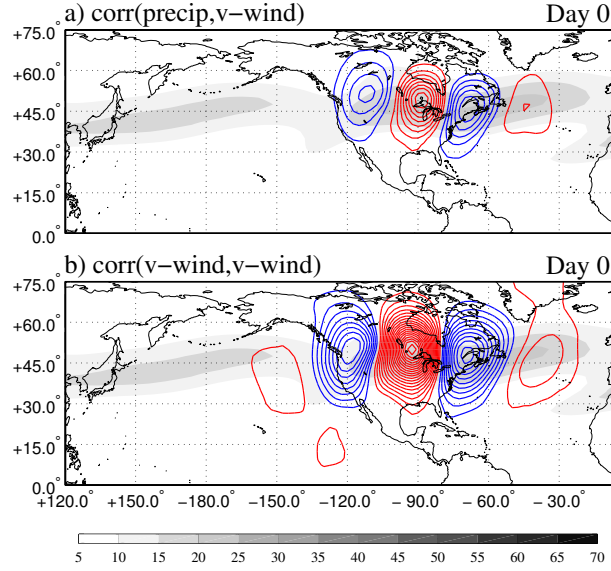


FIG. 7. Multi-model average day 0 July one-point correlation map between daily 300 hPa meridional wind anomalies at each grid cell and a base point of (a) daily precipitation averaged around five grid cells centered on the Lake Superior grid cell, 48°N, 272°E, and (b) daily 300 hPa meridional wind at 50.0°N, 267.5°E during 1961-2000. Contour interval is 0.05. Positive (negative) correlations are shown in red (blue), and the zero line is omitted. Shading indicates the multi-model average July 300 hPa zonal wind speed ( $\text{m s}^{-1}$ ) between 1961-2000. Correlation values greater/less than  $\pm 0.05$  are significant at the 95% confidence level, based on the Student's two-tailed t-test.

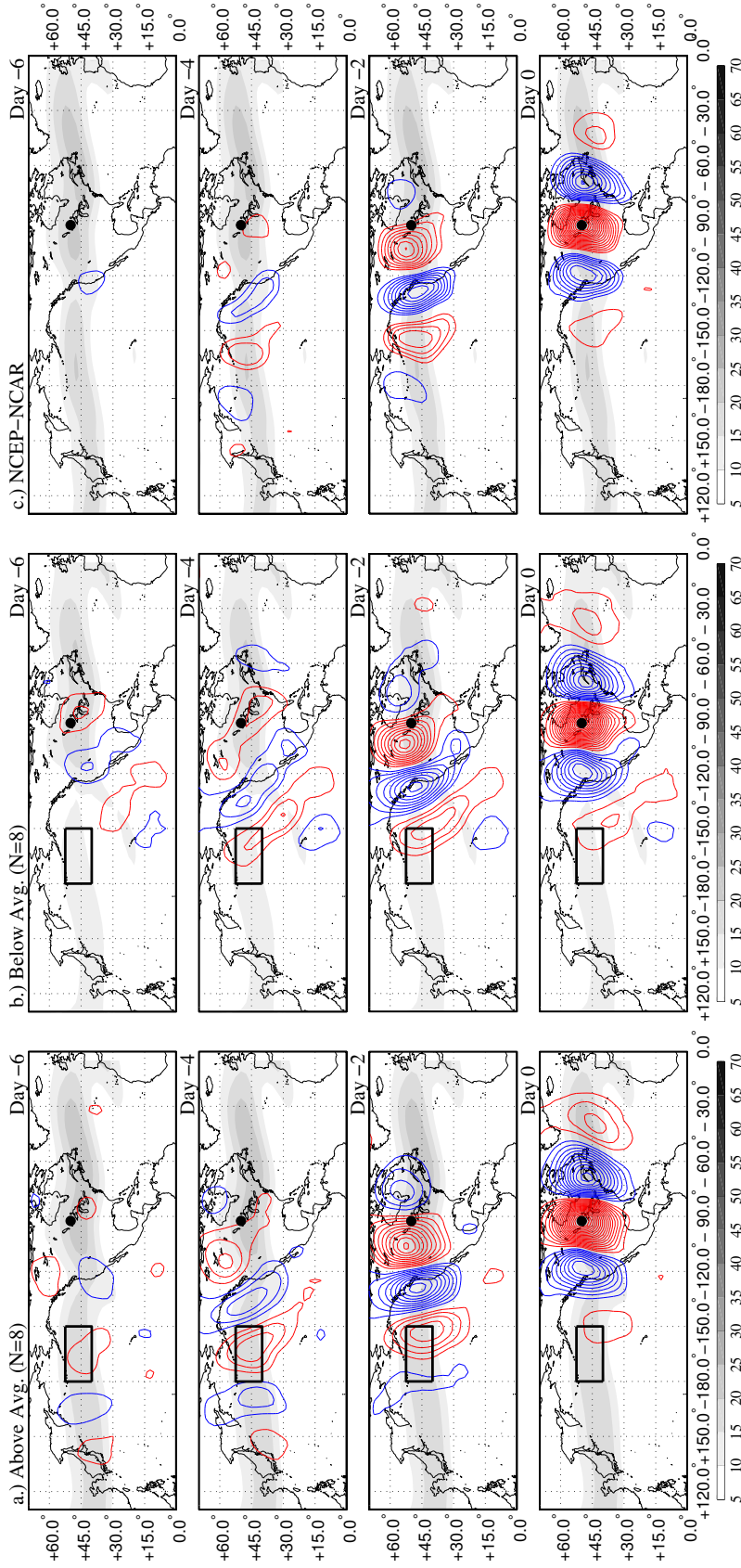


FIG. 8. Multi-model composite of July time-lag correlation maps (base point 50.0°N, 267.5°E; identified by the black dot) for models with (a) above- and (b) below-average 300 hPa zonal wind in the region outlined by the black box (40°-52.5°N and 180°-150°W) between 1961-2000. There are eight models in each pool. (c) Observed July time-lag correlation maps (contours) between daily 300 hPa meridional wind at 50.0°N, 267.5°E and 300 hPa meridional wind anomalies at every point between 180°-150°W and 60°-30°E. The contour interval is 0.05 and positive (negative) correlations are shown in red (blue). Shading represents the average 300 hPa zonal wind ( $\text{m s}^{-1}$ ) (a, b) among models and (c) from NCEP-NCAR reanalysis.

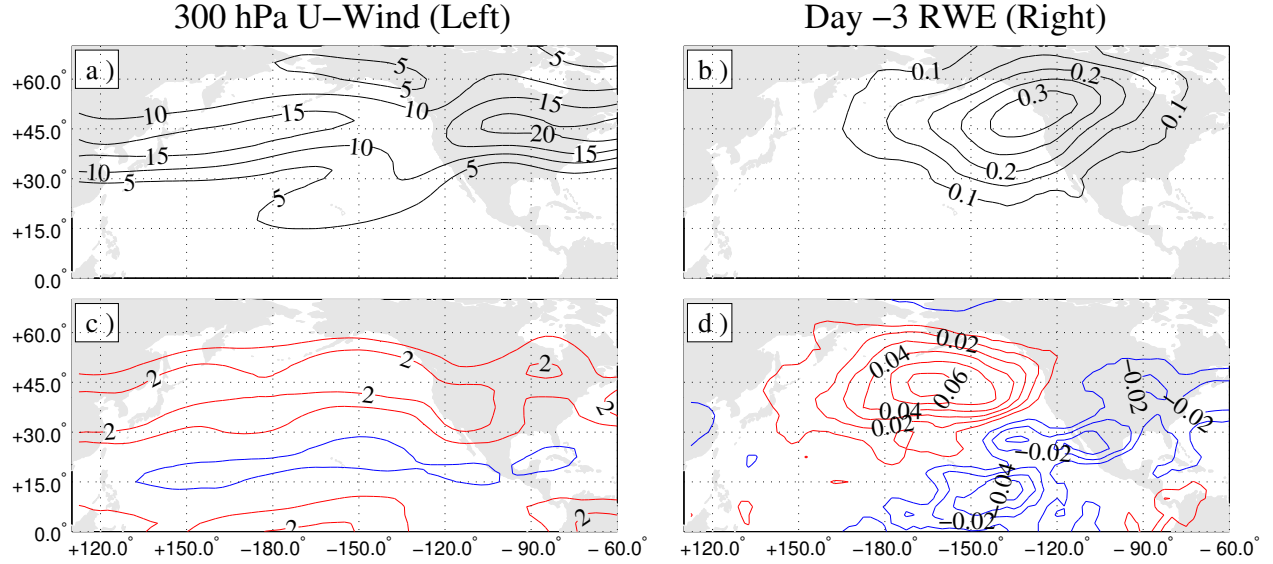


FIG. 9. July results from MCA of simulated 300 hPa zonal wind and day -3 RWEs. Multi-model average of mean July (a) 300 hPa zonal wind ( $\text{m s}^{-1}$ ) and (b) Day -3 RWE of one-point correlation map between 1961-2000. (c) Heterogeneous map of 300 hPa zonal wind regressed onto day -3 RWE expansion coefficients. Red (blue) contours represent positive (negative) perturbation isotachs in units of  $\text{m s}^{-1}$ , with the zero-line omitted. (d) Heterogeneous map of day -3 RWE patterns regressed onto 300 hPa zonal wind expansion coefficients. Red (blue) contours represent positive (negative) correlation perturbations in units of 0.01, with the zero-line omitted.

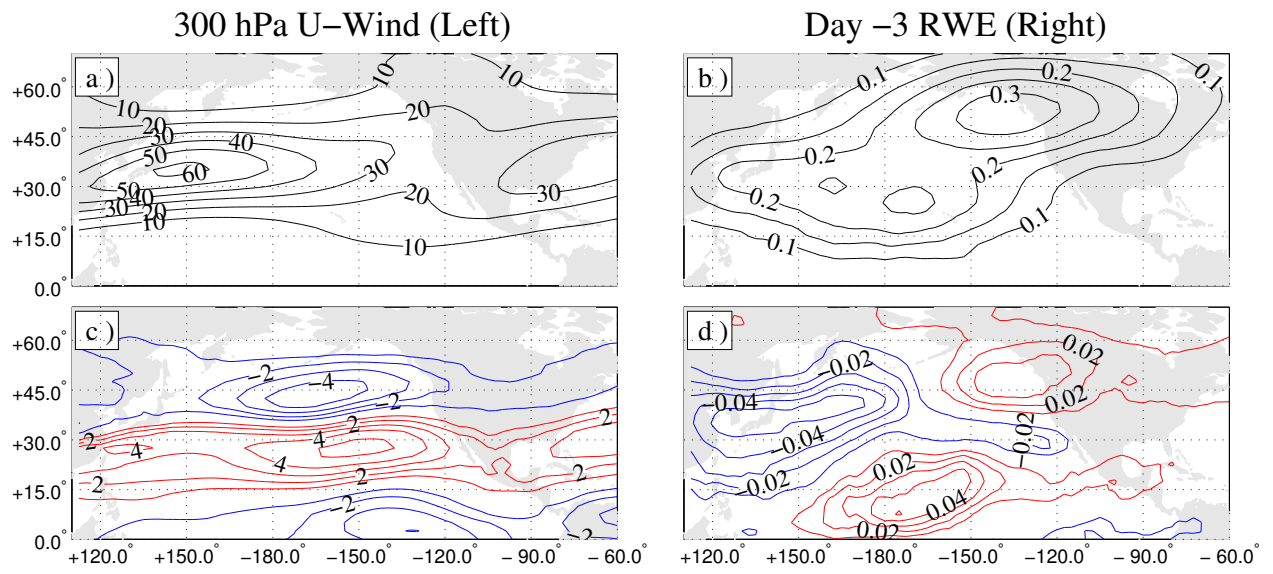


FIG. 10. Same as Fig. 9, except for December.

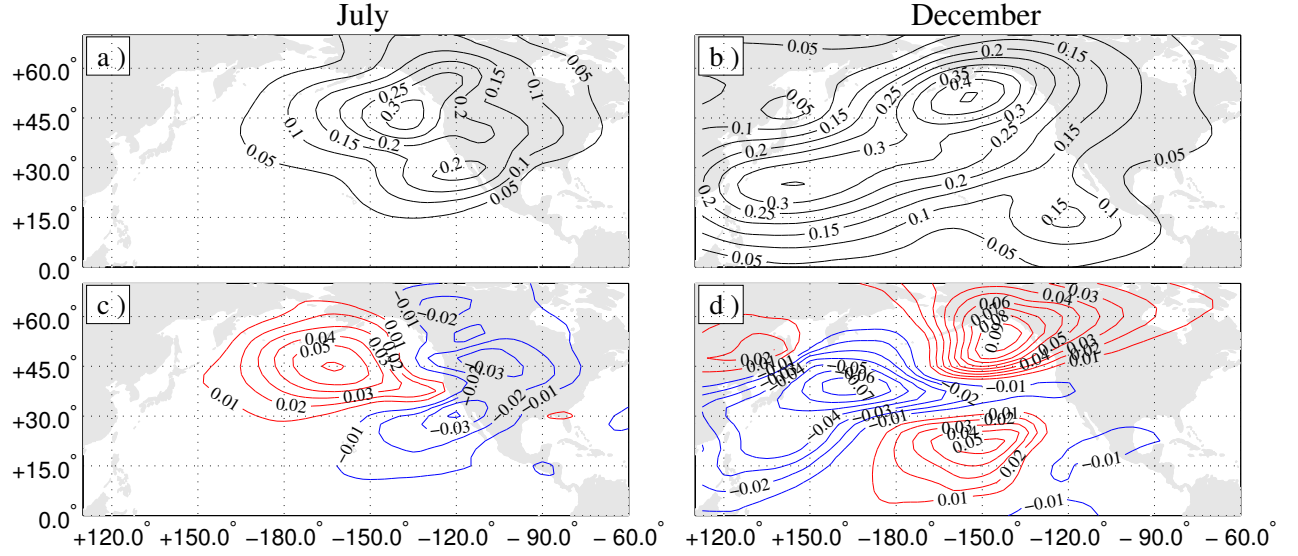


FIG. 11. (a) The RWE at day -3 from the barotropic model with a background state from the multi-model mean in July. (b) Same as (a) but for December. The contour interval is 0.05. (c) The July difference in RWE at day -3 from the barotropic model with background winds from the multi-model mean plus the MCA pattern and the barotropic model with background winds from the multi-model mean minus the MCA pattern. The pattern is divided by two to allow direct comparison with the MCA analysis. (d) Same as (c) but for December. Red (blue) contours represent positive (negative) values. The contour interval is 0.01, and the zero-line omitted.